applied sciences

MDPI

Article

Numerical Analysis on Flexural Behavior of Steel Fiber-Reinforced LWAC Beams Reinforced with GFRP Bars

Yijia Sun, Yang Liu, Tao Wu *, Xi Liu and Haodan Lu

School of Civil Engineering, Chang'an University, Xi'an 710061, China; sunyijiachd@163.com (Y.S.); 13891705608@163.com (Y.L.); lliuxii@163.com (X.L.); luhaodann@163.com (H.L.)

* Correspondence: wutaochd0922@yahoo.com; Tel.: +86-139-9132-2194

Received: 30 October 2019; Accepted: 22 November 2019; Published: 27 November 2019

Abstract: Three-dimensional nonlinear finite-element (FE) models using an explicit algorithm were established to simulate the behavior of beams reinforced with glass fiber-reinforced polymer (GFRP) bars cast using lightweight aggregate concrete (LWAC) with and without steel fibers, and the progressive damage model was employed to simulate the rupture of GFRP. The developed FE model was evaluated by test results, and it exhibited good agreement with the test results in terms of moment–deflection response, serviceability performance, ultimate capacity, and failure mode. Influencing factors, including the section height, reinforcement ratio, and span length were discussed according to the established FE model. It was revealed that the reinforcement ratio corresponding to balanced failure was higher than that given by code ACI 440.1R, which confirmed the necessity of the amplification factor of a balanced reinforcement ratio to ensure concrete crushing of the beam. For specimens that failed due to concrete crushing, the increase in fiber-reinforced polymer (FRP) reinforcement ratio did not significantly improve the ultimate capacity, but it did have an obvious effect on the reduction of deflection at service load. Moreover, a greater reinforcement ratio was needed for beams when the span length increased.

Keywords: lightweight aggregate concrete; steel fiber; fiber-reinforced polymer bar; finite element analysis (FEA); numerical analysis

1. Introduction

Lightweight aggregate concrete (LWAC) is beneficial for use in structures such as large-span bridges, high-rise buildings, and offshore oil platforms owing to its lower density, higher specific strength, and reliable durability [1,2]. However, the low strength of the aggregate negatively affected the tensile strength and brittleness of LWAC [3]. In recent years, the addition of steel fiber into mixtures of LWAC has received considerable attention for its higher tensile strength and better toughness comparatively to plain LWAC [4–8]. Fiber-reinforced polymer (FRP) bars are regarded as satisfactory alternatives to steel reinforcement in reinforced concrete (RC) structures due to their corrosion resistance, high strength-to-weight ratio, nonmagnetic, and nonconductive nature [9]. The combination of steel fiber-reinforced lightweight aggregate concrete (SFLC) and FRP is expected to be a promising system due to its prospectively desirable serviceability, high strength-to-weight ratio, and reduced overall lifetime cost [10].

The design of FRP–RC beams is usually governed by the requirements in the serviceability limit state due to the low elastic modulus of the FRP reinforcements [11,12]. Researchers have performed many investigations on FRP-reinforced fibrous concrete beams and proved the benefits of the fibers achieved in postcracking stiffness. Gribniak et al. [13] indicated that the tension–stiffness characteristics after the cracking of FRP–RC beams increased noticeably when steel fibers were used. Zhu et al. [14] carried out flexural tests on partially fiber-reinforced beams reinforced with FRP bars and concluded that the deflection of the specimens could be significantly reduced by adding steel fibers to the concrete. Abed and Alhafiz [15] investigated the effect of basalt microfibers on the flexural behavior of concrete beams reinforced with basalt fiber-reinforced polymer (BFRP) bars. They concluded that introducing basalt fibers to the concrete helped improve the curvature ductility and postcracking behavior of the beams. In recent research by the authors [10], the investigation on the flexural behavior of SFLC beams reinforced with glass fiber-reinforced polymer (GFRP) bars revealed that the specimens exhibited low deflection and high load-carrying capacity, and the specimens showed acceptable midspan deflections but greater crack widths compared to the limits recommended by the codes. However, the available information about the SFLC beams reinforced with GFRP bars is still incomplete. The factors affecting the performances of beams such as span length and reinforcement ratio need to be further studied.

In most cases, the finite element (FE) method can be a powerful instrument to complete the structural analysis [16,17]; nonetheless, one of main issues associated with the analysis of SFLC beams reinforced with GFRP bars is the nonlinear corporation system, which brings impediments on the convergence of frequently used implicit procedures. A dynamic explicit algorithm is salient for its calculation without iterations; as a result, the convergence problem brought by nonlinear behavior is abandoned. Concerning that it is capable of resolving the static problem when the entire loading period and each time increment are fully sufficient [18], the application of an explicit algorithm is considered as an excellent solution for the study of GFRP-reinforced SFLC beams.

This study was dedicated to establish three-dimensional nonlinear FE models for LWAC and SFLC beams reinforced with GFRP bars by using an explicit algorithm. The established models were evaluated by test results. Moreover, the effects of span length, height of section, and reinforcement ratio on the performance of beams were discussed.

2. Nonlinear Finite–Element Modeling

2.1. General

The nonlinear finite element implicit algorithm has been extensively used for the numerical analysis of reinforced concrete structures and members. However, the implicit algorithm may not perform well when it is used to resolve complex nonlinear problems, while the explicit procedure is a better method for models involving complex cracking and damage behaviors.

The nonlinear behavior of LWAC, which is widely known for its brittleness, is especially obvious after cracking, which would lead to severe convergence difficulties if the implicit procedure is applied. An excellent feature of the explicit algorithm is that the global stiffness matrix is not necessary, whereby the processes of iterations and convergence requirement are abandoned. In explicit procedures, the displacements, velocities, and accelerations at the beginning of the increment collectively contribute to the state of the models at the end of the increment. Thus, reliably small increments are a prerequisite of an accurate and stable calculated result. Furthermore, iterative calculation for a stiffness matrix is no longer required in an explicit algorithm [18]; accordingly, if the model has a large number of degrees of freedom, the application of the explicit method will result in a reduction in calculation cost.

2.2. Finite-Element Geometry and Mesh

Figure 1 shows the FE model developed in the ABAQUS software (SIMULIA corp, Providence, Rhode Island, USA). In this study, the symmetry was not considered so that more of the information contained in finite element models could be obtained. To obtain a regular mesh grid, structured meshing tech was used to model the concrete, and considering the relatively large calculation cost of the explicit procedure, the reduced integration element was employed. It is worth noting that a single block element with reduced integration has only one integral point, which suggests that more elements are required to ensure the precision of whole FE model in this case. Therefore, for the purposes of saving cost and ensuring the accuracy of the model, the C3D8R-type element was assigned to the concrete component, and a relatively small dimension (25 mm) was adopted for the concrete elements. For the steel and GFRP bars, T3D2 (3D-2 nodes linear truss) elements were chosen to complete the modeling process, and their length was selected as twice that of the concrete element. The bond between reinforcing bars and concrete was assumed to be perfect by using embedded region tech, whereas the stress transfer of bond–slip behavior was considered by defining the tension stiffening of concrete properties.

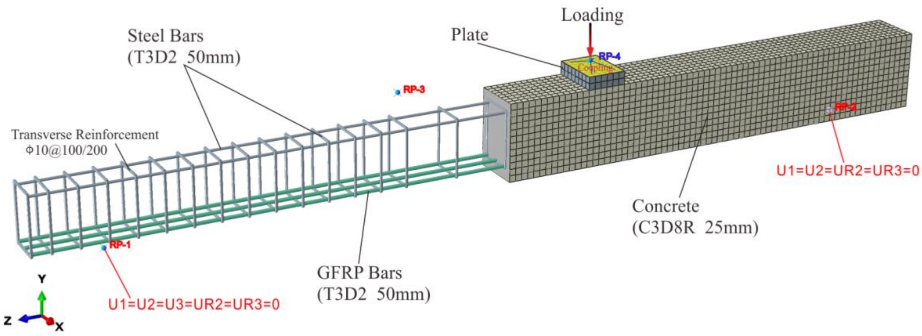

Figure 1. Finite element models developed by present study.

2.3. Boundary Conditions and Load Application

To prevent the unexpected stiffening brought by using constraint methods such as tie and coupling [19], two rigid plates with similar size to the supports used in the tests were applied for the FE models. The properties of the interactions between the plates and concrete were defined by hard contact and the Coulomb friction referring to the normal and tangential contact behaviors, respectively.

The degrees of freedom corresponding to the out-of-plane factors of the four loaded reference points were blocked. For instance, to simulate the in-plane sliding support, the loaded point RP-2 was blocked in the directions of U1, U2, UR2, and UR3. Details of the boundary conditions are indicated in Figure 1.

The dynamic explicit procedure requires a fairly slow loading rate to simulate the quasi-static situation, in addition to the smoothness of changes in the velocity and displacement. To this end, the smooth step was used to define the loading system. This tech is capable of generating an amplitude that has first and second derivatives of zero at two ends of a given time period, as shown in Figure 2.

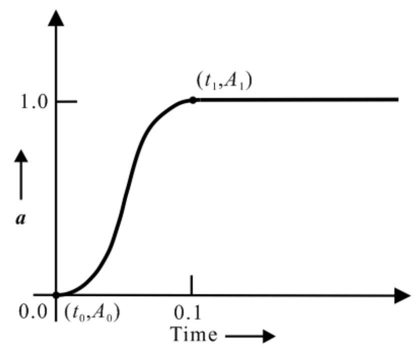

$$\boldsymbol{a} = \begin{cases} A_0 & \text{for } t \le t_0 \\ A_0 + (A_1 - A_0)\xi^3 (10 - 15\xi + 6\xi^2) & \text{for } t_0 < t < t_1 \\ A_1 & \text{for } t \ge t_0 \end{cases}$$

$$\text{where } \xi = \frac{t - t_0}{t_1 - t_0}$$

Figure 2. Smooth step amplitude definition example with two given data points.

2.4. Dynamic Explicit Solution Scheme

The motion equation and its relevant initial conditions in explicit procedures can be expressed as follows:

$$M\ddot{u} + C\dot{u} + Ku = P(t) \tag{1}$$

$$u(t=0) = u_0 \tag{2}$$

$$\dot{u} = \frac{\partial u}{\partial t}|_{t=0} = v_0 \tag{3}$$

$$\ddot{u} = \frac{\partial u^2}{\partial^2 t}|_{t=0} = a_0 \tag{4}$$

where M, C, and K are the mass, damping, and stiffness matrixes, respectively; t is the time; u, $\dot{u}$, and $\ddot{u}$ denote the displacement, velocity, and acceleration, respectively; u_0, v_0, and a_0 are the displacement, velocity, and acceleration at $t = 0$, respectively; and $P(t)$ is the nodal forces vector.

During the explicit procedures, the displacements are solved by using the central difference method, and the basic equation can be derived as:

$$\dot{u}\Big|_{(t+\frac{\Delta t}{2})} = \dot{u}\Big|_{(t-\frac{\Delta t}{2})} + \frac{(\Delta t\big|_{(t+\Delta t)} + \Delta t\big|_{(t)})}{2}\ddot{u}\Big|_{(t)} \tag{5}$$

$$u\Big|_{(t+\Delta t)} = u\Big|_{(t)} + \Delta t\Big|_{(t+\Delta t)}\dot{u}\Big|_{(t+\frac{\Delta t}{2})} \tag{6}$$

where Δt is the time increment.

The state of the model at time step t_i is directly derived from the previous step t_{i-1} so that an accurate result can be obtained if the increments are small enough. Nonetheless, the highly nonlinear behavior of LWAC results in variation of the highest frequency of the model, which would lead to a varying smallest stable temporal increment. Consequently, inconsistent time increments are requested. In fact, the central difference operator is conditionally stable, and the stability limit for the operator is given in terms of the highest of frequency of the system as (with no damping):

$$\Delta t \leq \frac{2}{\omega_{\max}} \tag{7}$$

where $\omega_{\max}$ is the highest frequency of the system.

With damping, the stable time increment is given by:

$$\Delta t \leq \frac{2}{\omega_{\max}}\left(\sqrt{1+\xi_{\max}^2} - \xi_{\max}\right) \tag{8}$$

where $\xi_{\max}$ is the fraction of critical damping in the mode with the highest frequency.

During the explicit procedure, an element-by-element method was used to estimate the stability limit for time increment, which is expressed as:

$$\Delta t \approx \min\left(L_e\sqrt{\frac{\rho}{\hat{\lambda}+2\hat{\mu}}}\right) \tag{9}$$

where L_e is the element dimension, ρ is the density of the material in the element, $\hat{\lambda}$ and $\hat{\mu}$ are effective Lame's constants for the material.

Additionally, hereinto a small amount of damping is introduced in the form of bulk viscosity to control high-frequency oscillations, which is contrary to the usual engineering intuition. The bulk viscosity was introduced with truncation frequency damping. It generates a bulk viscosity pressure P_{bv1} that is linear in the volumetric strain rate:

$$p_{bv1} = b_1 \rho c_d L_e \varepsilon_{vol} \tag{10}$$

where b_1 is the damping coefficient of 0.06, c_d is the current dilatational wave speed, and ε_{vol} is the volumetric strain rate.

2.5. Material Model

To explicitly track the overall behavior of steel-reinforced LWAC beams reinforced with GFRP bars, the concrete damaged plastic (CDP) model and elastoplastic model along with progressive damage available in Abaqus were used to simulate the mechanical properties of LWAC and GFRP bars, respectively. Especially, parameters required by the tensile behavior of the CDP model and those needed by the progressive damage model were adjusted according to the demand of analysis.

2.5.1. CDP Model

The concrete damaged plastic (CDP) model [19–21] assumed compressive and tensile failure as two failure mechanisms. The yield surfaces and deviatoric plane of the CDP model are shown in Figure 3. The yield function of the CDP model is depicted as [19] follows:

$$F = \frac{1}{1-\alpha}[\overline{q} - 3\alpha\overline{p} + \beta(\tilde{\varepsilon}_t^{pl}, \tilde{\varepsilon}_c^{pl})\langle\hat{\sigma}_{\max}\rangle - \gamma\langle-\hat{\sigma}_{\max}\rangle] - \overline{\sigma}_c(\tilde{\varepsilon}_c^{pl}) \tag{11}$$

$$\overline{p} = -\frac{1}{3}\mathrm{tr}(\boldsymbol{\sigma}) \tag{12}$$

$$\overline{q} = \sqrt{\frac{3}{2}\|\mathrm{dev}(\boldsymbol{\sigma})\|} \tag{13}$$

with

$$\alpha = \frac{(\sigma_{b0}/\sigma_{c0}) - 1}{2(\sigma_{b0}/\sigma_{c0}) - 1}; \qquad 0 \leq \alpha \leq 0.5 \tag{14}$$

$$\beta = \frac{\overline{\sigma}_c(\tilde{\varepsilon}_c^{pl})}{\overline{\sigma}_t(\tilde{\varepsilon}_t^{pl})}(1-\alpha) - (1+\alpha) \tag{15}$$

$$\gamma = \frac{3(1-K_c)}{2K_c - 1} \tag{16}$$

where $\overline{p}$ and $\overline{q}$ are the hydrostatic stress and the von Mises equivalent stress, respectively; $\tilde{\varepsilon}_t^{pl}$ and $\tilde{\varepsilon}_c^{pl}$ are the plastic strain in tension and compression, respectively; $\hat{\sigma}_{\max}$ is the max principal effective stress; $\boldsymbol{\sigma}$ denotes the stress tensors; σ_{b0}/σ_{c0} is the initial equi-biaxial compressive yield stress to initial uniaxial compressive yield stress, which was taken as 1.16 in this study. $\overline{\sigma}_c(\tilde{\varepsilon}_c^{pl})$ and $\overline{\sigma}_t(\tilde{\varepsilon}_t^{pl})$ are cohesion values in tension and compression, assumed to depend on the compressive and tensile equivalent plastic strains, $\tilde{\varepsilon}_c^{pl}$ and $\tilde{\varepsilon}_t^{pl}$, respectively.

As shown in Figure 3, K_c is the ratio of the second stress invariant on the tensile meridian to that on the compressive meridian, which directly controls the shape of the yield surfaces in the deviatoric plane. According to the work of Lubliner [20], K_c was taken as 2/3 in this study.

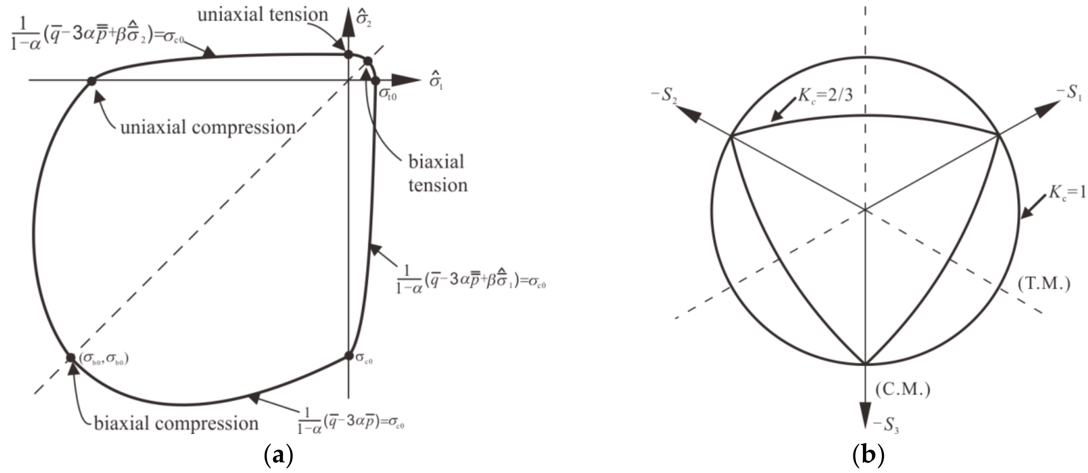

Figure 3. Illustration of the yield surfaces and deviatoric plane of the concrete damaged plastic (CDP) model [19]: (**a**) Yield surfaces of the CDP model; (**b**) Deviatoric plane of the CDP model (σ_{t0} is the tensile stress corresponding to the end of the linear portion in the ascending branch).

2.5.2. Compressive Stress–Strain Relationship

The stress–strain models proposed by the authors [22] for plain LWAC and SFLC were introduced in the FE model, which was expressed as follows.

Ascending:

$$y = ax + (3-2a)x^2 + (a-2)x^3 \tag{17}$$

Descending:

$$y = \frac{k_1 \lambda x}{k_1 \lambda - 1 + x^{k_2 \lambda}} \tag{18}$$

where $y = f/f_c{}'$; $x = \varepsilon/\varepsilon_c$; f_1 is the general stress in the compression; ε_1 is the general strain in the compression; $f_c{}'$ is the peak stress; ε_c is the strain corresponding to the peak stress; E_c is the elastic modulus of the concrete; and a, λ, k_1, and k_2 are the modified factors, as defined in Table 1.

Table 1. Parameters for compressive stress–strain model. LWAC: lightweight aggregate concrete, SFLC: steel fiber-reinforced lightweight aggregate concrete.

Parameters	LWAC	SFLC [1]
a	$1.797E_c\varepsilon_c/f_c' - 1.264$	
λ	$1/[1-(f_c'/\varepsilon_c E_c)]$	
k_1	$k_1 = (37.15/f_c')^{3.062}$	$k_1 = -0.220r - 0.017f_c' + 1.758$
k_2	$k_2 = (41.25/f_c')^{1.544}$	$k_2 = 0.299r + 0.014f_c' - 0.505$

[1] r = volume fraction of steel fibre in %.

The conversions established by Carreira and Chu [23] were employed to generate the modified compressive stress–strain model. The expressions for the initial modulus of elasticity and strain corresponding to peak stress can be written as:

$$E_c = 0.0736(f_c')^{0.3}{\rho_d}^{1.51} \tag{19}$$

$$\varepsilon_c = (0.71f_c' + 168) \times 10^{-5} \tag{20}$$

where ρ_d is the oven-dry density of concrete.

2.5.3. Tensile Behavior

Hillerborg described the tensile behavior of plain concrete using tension stress and crack width [24], which gives rise to a linear descending portion for the tension constitutive curves. However, the 'tension stiffening' that reflects the stress transfer between rebar and concrete cannot be neglected. In the present study, considering the different bond characteristics of GFRP bars compared to traditional steel reinforcing bars, and by conducting trial calculations previously to this study, a rapidly decreased portion was assumed after the tensile strength (f_t) of plain LWAC, while a final 10 times peak strain (ε_{t0}) was adopted for all models, as suggested by [19]. The diagram of uniaxial tension behavior of concrete is depicted in Figure 4.

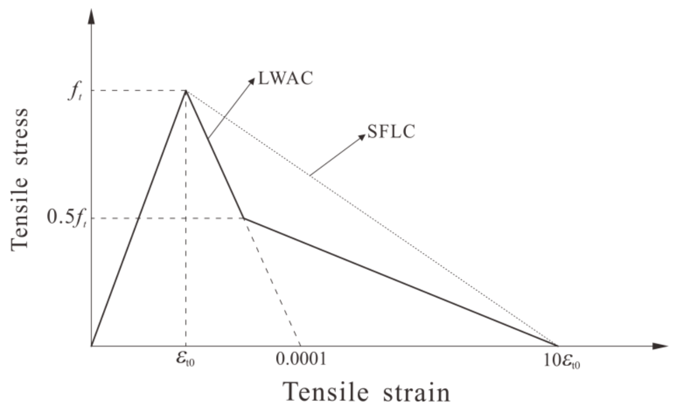

Figure 4. Post failure stress–fracture energy curve.

2.5.4. Damage Evolution

The definition of damage parameter in the CDP model is demonstrated in Figure 5, where the plastic strain in tension and compression were calculated as:

$$\tilde{\varepsilon}_c^{pl} = \tilde{\varepsilon}_c^{in} - \frac{d_c}{(1-d_c)}\frac{\sigma_c}{E_c} \tag{21}$$

$$\tilde{\varepsilon}_t^{pl} = \tilde{\varepsilon}_c^{ck} - \frac{d_t}{(1-d_t)}\frac{\sigma_t}{E_c} \tag{22}$$

where d_c and d_t are the compressive and tensile damage parameter, respectively; $\tilde{\varepsilon}_c^{in}$ is the (inelastic) crushing strain, and $\tilde{\varepsilon}_t^{ck}$ is the cracking strain (Equation (23)).

$$\begin{aligned} \tilde{\varepsilon}_c^{in} &= \varepsilon_c - \tfrac{\sigma_c}{E_c} \\ \tilde{\varepsilon}_t^{ck} &= \varepsilon_t - \tfrac{\sigma_t}{E_c} \end{aligned} \tag{23}$$

The definition of the damage parameter does not affect macro responses such as the moment–deflection and crack patterns; therefore, with the purpose of saving calculation costs, a simple, linear damage evolution was assumed in the present study, which can be written as:

$$d_i = 1 - \frac{\sigma_i}{f_i}; i = t, c \tag{24}$$

where t and c represent tension and compression, respectively; σ is the general stress in each time increment, and f is the peak stress.

Furthermore, to ensure the stability of models, damage parameters in both the compression and tension were limited to below 0.8, resulting in a predetermined residual stress of approximately 20% peak stress.

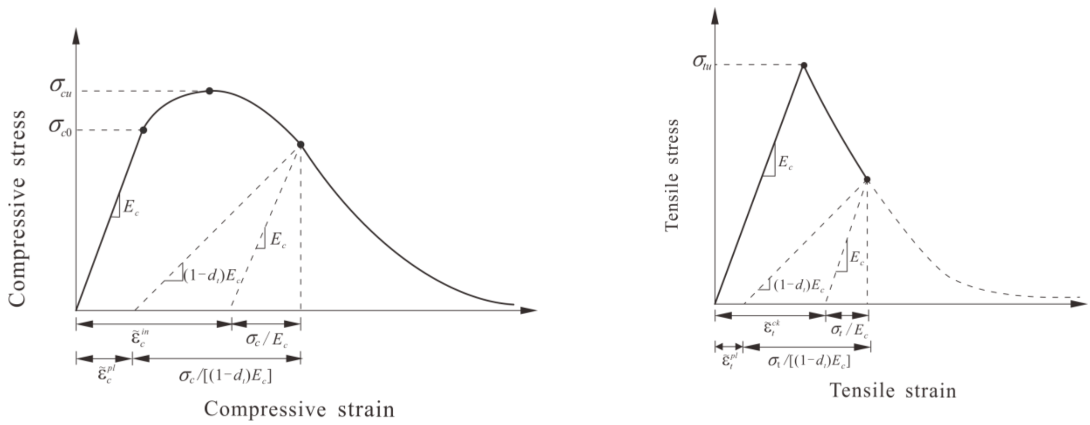

(**a**) (**b**)

Figure 5. Indication of damage evolution in compression and tension: (**a**) Damage evolution in compression; (**b**) Damage evolution in tension (σ_{cu} and σ_{tu} are the compressive and tensile strength, respectively).

2.5.5. Modeling of GFRP and Steel Bars

Bilinear behavior was applied to the GFRP and steel bars, which includes linear elastic and hardening plastic branches in the stress–strain curve. The sudden rupture of GFRP bars is one of the significant observations of the experimental investigation. To incorporate this phenomenon into the FE models, progressive damage was introduced into the stress–strain relationship of GFRP bars. Figure 6 presents the progressive damage model used, where $\bar{\varepsilon}_0^{pl}$ was taken as the end of the linear segment, while $\bar{\varepsilon}_f^{pl}$ was defined as a value that almost equals to zero, such as 0.00001, by which the linear behavior up to failure could be simulated.

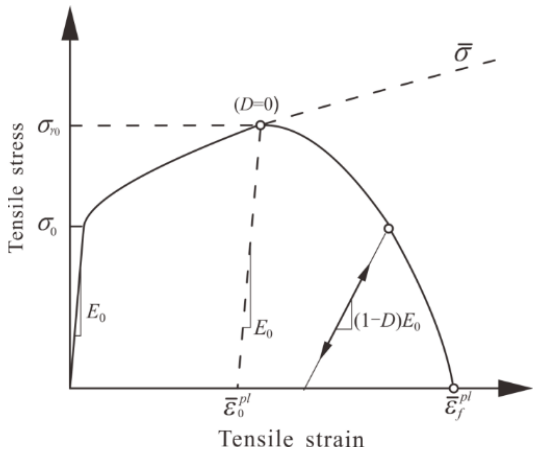

Figure 6. Indication of stress–strain curve including progressive damage (E_0 is the initial elastic modulus; σ_0 is the stress corresponding to end of the elastic stage; and σ_{r0} is the stress at the onset of damage).

3. Experimental Tests

3.1. Material and Specimens

The performance of FE models developed in this paper is validated against the experimental tests previously conducted by the authors [10]. A total of 10 LWAC specimens tested under four-point bending loads were presented. The expanded shale type of lightweight aggregate with a maximum size of 16 mm was used as the coarse aggregate. The test parameters were: (1) GFRP reinforcement ratio ρ_f; (2) steel fiber content; (3) bar diameter d_b; and (4) type of reinforcement. The details of the specimens are reported in Figure 7 and Table 2. The mechanical properties of the GFRP and steel bars determined by tests according to ACI 440.3R [25] and ASTM E8/E8M [26], respectively, are shown in Table 3.

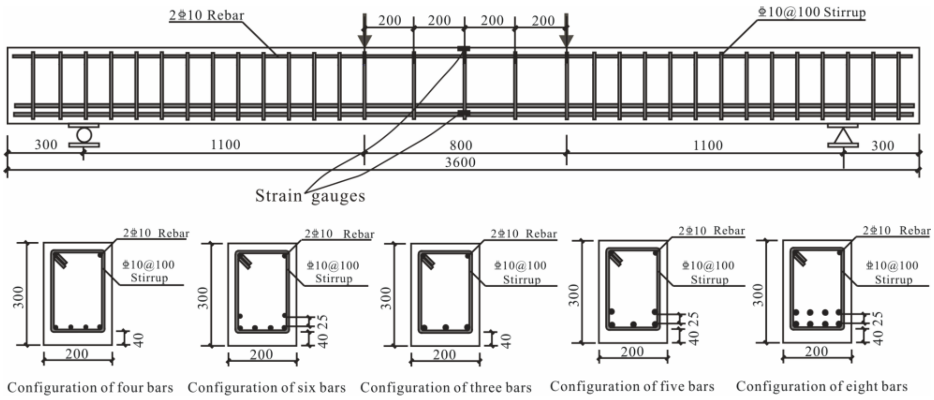

Figure 7. Reinforcement details of specimens.

Table 2. Details and experimental results of specimens.

Series	Specimens ID	f_{cu} (MPa)	ρ_f (%)	M_u (kN·m)	Δ_s(mm)	$E_f A_f$ (kN)	Failure Mode [1]
Series I	LC–G–5#13.77	64.7	1.64	82.92	15.0	33,027	C.C
	SLC–G–5#13.77	82.3	1.64	98.75	11.3	33,027	B.F
	LC–G–8#13.77	62.5	2.66	97.96	12.5	52,843	C.C
	SLC–G–8#13.77	79.4	2.66	119.85	13.1	52,843	C.C
Series II	LC–G–3#13.77	54.9	0.92	63.51	13.3	19,816	B.F
	SLC–G–3#13.77	81.6	0.92	73.54	7.1	19,816	FRP.R
	LC–G–6#9.87	64.4	0.98	43.30	6.6	21,452	FRP.R
	SLC–G–6#9.87	69.5	0.98	56.51	4.1	21,452	FRP.R
Series III	LC–G–4#9.87	61.6	0.62	32.52	1.2	14,302	FRP.R
	LC–S–4#10.62	76.2	0.72	47.77	-	65,974	C.C

[1] C.C = Concrete crushing, B.F = Balanced failure, FRP.R = FRP rupture; f_{cu} = cube compressive strength of concrete; E_f = modulus of elasticity of the glass fiber-reinforced polymer (GFRP) bars; A_f = area of tension reinforcement.

Table 3. Properties of GFRP and steel bars.

Type	d_b (mm)	A_f (mm^2)	E_f (GPa)	f_{fu} (MPa)	ε_{fu} (%)
GFRP–1	9.87 ± 0.08	76.5	47	663	1.42
GFRP–2	13.77 ± 0.13	148.8	44	602	1.33
Steel	10.62 ± 0.05	78.5	E_s = 204	f_y = 445	ε_y = 2.28

[1] E_s = modulus of elasticity of the steel rebars; f_{fu} = ultimate tensile strength of the GFRP bars; f_y = yield strength of the steel rebars; ε_{fu} = ultimate tensile strain of the GFRP bars; ε_y = ultimate tensile strain of the steel rebars.

The symbols "LC" and "SLC" denote the types of concrete. "G" denotes GFRP bars, while "S" denotes steel reinforcements. The final part of each label demonstrates the number and diameter of the reinforcing bars. For instance, SLC–G–3#9.87 represents a SFLC specimen that was reinforced with three GFRP bars with a diameter of 9.87 mm.

3.2. Test Results

3.2.1. Failure Mode

The test results including ultimate moments (M_u), failure modes, and deflections at 30% of M_u (Δ_s) are shown in Table 2. The typical failure modes of the specimens are given in Figure 8. Three typical failure modes were observed among the 10 specimens, namely, concrete crushing, balanced failure, and the rupture of GFRP bars. This result was corroborate with those of FRP-reinforced plain and fibrous normal weight concrete beams [27–29]. Specimens undergoing concrete crushing failure exhibited large deflection and crack widths in the midspan, and owing to its relatively gradual process, the damage incurred by this type of failure is less destructive than that of the other failure modes (Figure 8a). The balanced failure mode featured concrete crushing followed immediately by the rupture of GFRP bars. The concrete on the top surface at the midspan was compressed to crushed, and the beams collapsed along the crack caused by the sudden fracture of the GFRP bars, as shown in Figure 8b. Compared to the balanced failure, a distinct characteristic of the FRP rupture failure was that the concrete located in the compression zone was not crushed (Figure 8c). Hence, this type of failure involved fracturing without prior warning. Specimens that were classified into FRP rupture possessed relatively little deflection.

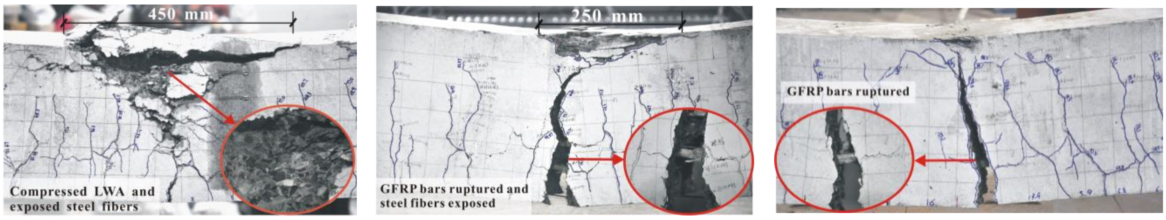

(a) (b) (c)

Figure 8. Typical failure of specimens: (**a**) Concrete crushing; (**b**) Balanced failure; and (**c**) Rupture of fiber-reinforced polymer (FRP) bars.

3.2.2. Moment–Deflection Relationship

The moment–deflection curves of the beams are displayed in Figure 9. All the FRP-reinforced beams yielded typical bilinear relationships before the peak load, namely, a steep linear stage that described the uncracked condition and a basically linear stage that represented the reduced postcracking stiffness. Similar observations were reported for FRP-reinforced normal weight concrete (NWC) beams with and without fibers [30]. For beams SLC–G–5#13.77 and SLC–G–8#13.77, the slopes of the deflection curves slightly decreased just before the peak load. It could be explained by the fact that the presence of the steel fiber restrained the propagation of the transverse cracks in the compression zone.

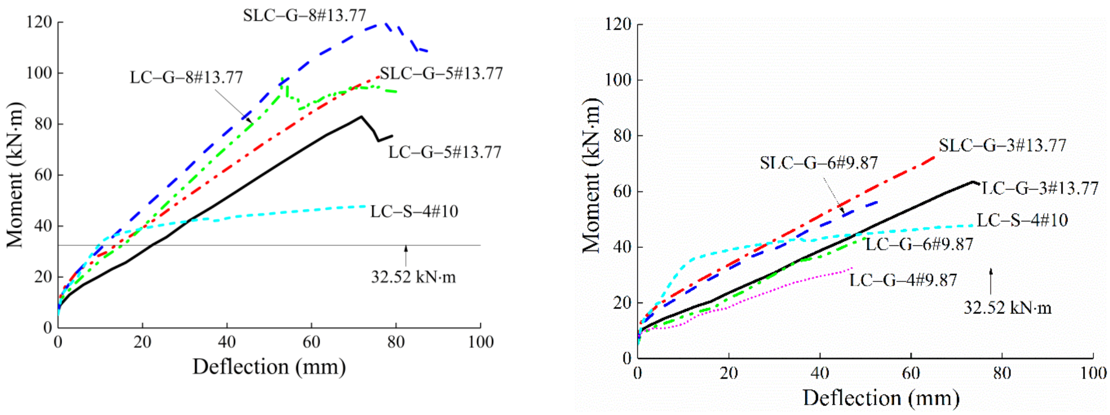

(a) (b)

Figure 9. Experimental moment–deflection relationships: (**a**) Series I; and (**b**) Series II and III.

Furthermore, for FRP-reinforced specimens that were damaged by concrete crushing, a nonlinear stage that corresponded to the crushing process was observed after the peak load. In this stage, the specimens continued to sustain the load with increasing deformation. The inelastic deformations near failure lent a degree of ductility for this failure mode, which was in agreement with the results reported for GFRP-reinforced NWC beams with and without fibers [27].

3.2.3. Deflection at Service Load

Bischoff et al. [31] recommended a load corresponding to 30% of M_u as a service load for FRP-reinforced beams. The Δ_s of the GFRP-reinforced beams are displayed in Figure 10. Specimens failed by concrete crushing and balanced failure yielded higher Δ_s than those of beams damaged by FRP rupture due to their higher M_u. The addition of the steel fiber contributed to decreasing the Δ_s for beams with low ρ_f values (0.92%–1.64%), but caused an increase in the Δ_s for that with ρ_f of 2.66%. GB 50608 [32] specified a deflection limit of L/200 (15 mm), according to which the beams exhibited conservative Δ_s except for specimen LC–G–5#13.77.

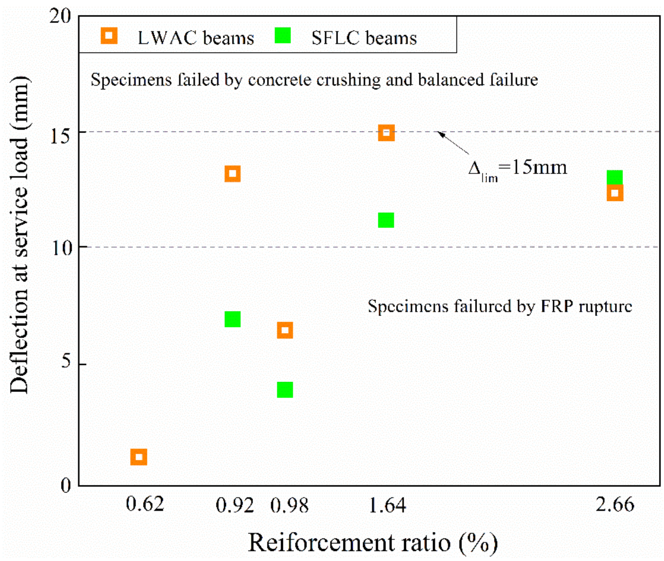

Figure 10. Deflections at service load.

3.2.4. Moment–FRP Strain Relationship

The applied moment versus the FRP strain is presented in Figure 11. The FRP bars assumed little deformation before the cracking moment was reached, indicating that the load was mainly sustained by concrete in the precracking stage. After cracking, the moment–FRP strain curves of FRP bars increased with reduced slope until failure.

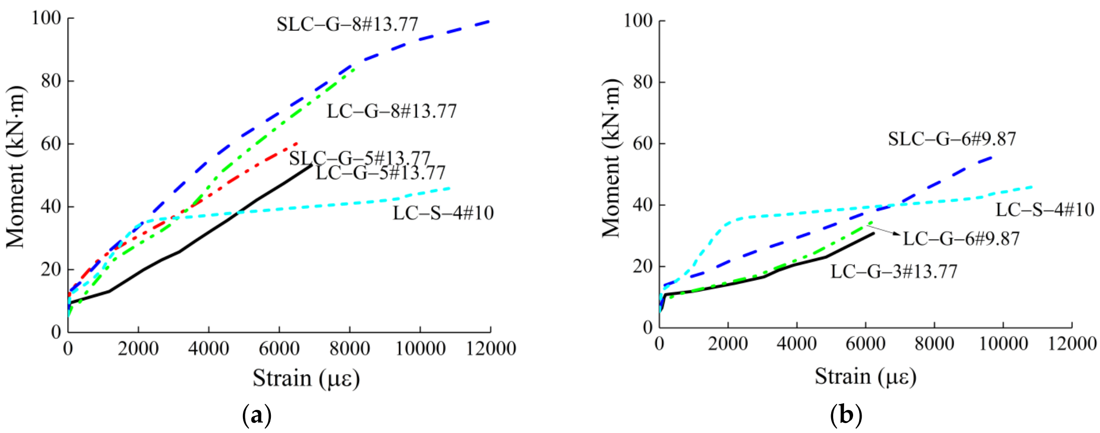

Figure 11. Moment–deflection relationship: (**a**) Series I; (**b**) Series II and III.

4. Validation of the Established FE Models

4.1. Failure Mode and Crack Pattern

The results predicted by the developed FE method are listed in Table 4. The failure models for all the tested beams were accurately predicted, indicating the inclusion of progressive damage into the properties of GFRP bars was capable of reflecting the rupture behavior in FE analysis. Typical failure shapes for each mode are depicted in Figures 12–15.

Table 4. Results predicted by the finite-element (FE) method.

Models	Moment		Deflection		Failure Mode
	M_u (kN·m)	$M_{u,\mathrm{Exp}}/M_{u,\mathrm{FEM}}$	Δ_s (mm)	$\Delta_{s,\mathrm{Exp}}/\Delta_{s,\mathrm{FEM}}$	
LC–G–5#13.77	71.69	1.16	12.82	1.17	C.C
SLC–G–5#13.77	82.96	1.19	14.13	0.79	B.F
LC–G–8#13.77	84.04	1.17	12.79	0.97	C.C
SLC–G–8#13.77	105.45	1.14	14.60	0.89	C.C
LC–G–3#13.77	58.38	1.09	10.91	1.22	B.F
SLC–G–3#13.77	63.26	1.16	6.39	1.11	FRP.R
LC–G–6#9.87	54.09	0.80	4.89	1.35	FRP.R
SLC–G–6#9.87	65.63	0.86	3.04	1.34	FRP.R
LC–G–4#9.87	44.81	0.73	1.17	1.02	FRP.R
LC–S–4#10.62	42.73	1.12	0.97	-	C.C
Mean	-	1.04	-	1.09	-
Standard deviation	-	0.17	-	0.19	-

4.1.1. Concrete Crushing for Steel Reinforced Beam

Crack patterns and damage distribution of steel reinforced beam LC–S–4#10.62 referring to the status of M_u are shown in Figure 12. It was observed that the possible cracks extended from 40% to 80% of the beam depth, which was close to test results. When the ultimate load was reached, the concrete elements located at the top surface of the midspan assumed a high degree of compressive damage. It can be concluded that the whole loading process and the final failure mode of the FE model for the steel-reinforced LWAC beam were greatly consistent with the observations obtained in tests.

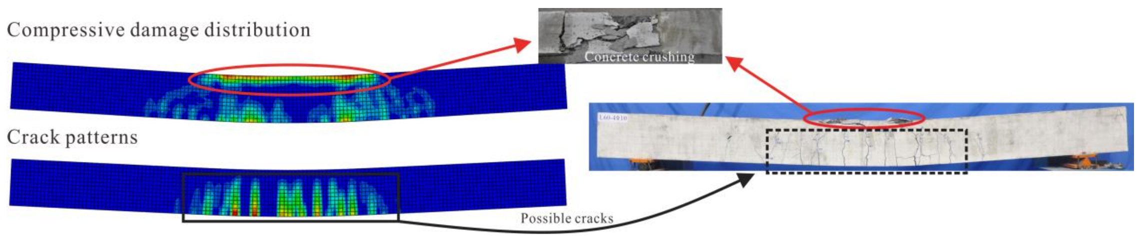

Figure 12. Crack patterns and failure modes of FE model LC–S–4#10.62.

4.1.2. Concrete Crushing for GFRP-Reinforced Beam

Specimen LC–G–5#13.77 was used to illustrate the failure of concrete crushing for GFRP-reinforced beams; the relevant crack patterns and failure modes are shown in Figure 13. Compared to the FE model for steel reinforced beams, the model for specimen LC–G–5#13.77 exhibited a larger possible cracking area along the span direction. Similar to the test results, diagonal cracks in the shear span were observed in the FE model, although their inclinations were relatively small. At the point that M_u was reached, the compressive damage initially occurred among the concrete elements at the top of the midspan. With further increasing of displacement, no significant decrease in the load was observed before total disintegration of the compressive concrete occurred, which was in good agreement with the experimental observation. In this stage, the strain in the GFRP bars continued to increase, as depicted in Figure 13b.

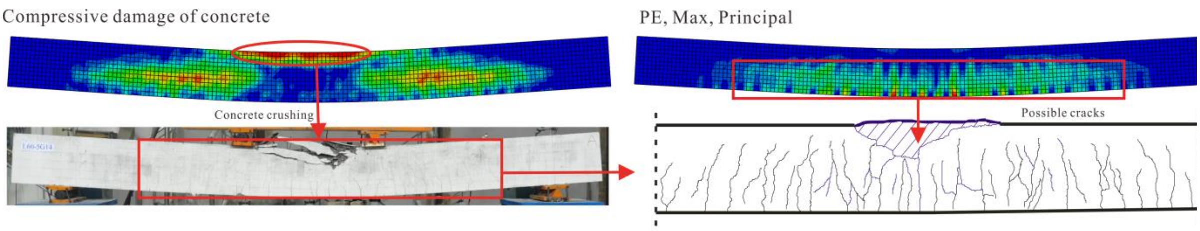

(**a**)

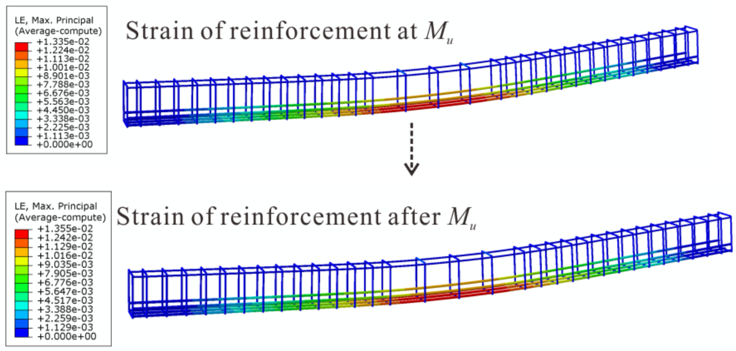

(**b**)

Figure 13. Crack patterns, failure modes, and strain of GFRP bars of FE model LC–G–5#13.77: (**a**) Failure mode and crack patterns; (**b**) Evolution of reinforcement strain.

4.1.3. Balanced Failure

Figure 14 presents the crack patterns, strain of GFRP bars, and final failure mode of the FE model for beam SLC–G–5#13.77. The length of the possible cracks ranged from 50% to 80% of the beam depth, and it can be observed that their distribution in this model was similar to that in the FE model for LC–G–5#13.77. Both models assumed a relatively longer range than that in the steel reinforced beam LC–S–4#10.62, which was considered to be a result of the low elastic modulus of the GFRP bars. Similar to the test results, the failure of the FE model began with the crushing of the concrete located on the top surface at the midspan, which was immediately followed by the rupture of the GFRP bars.

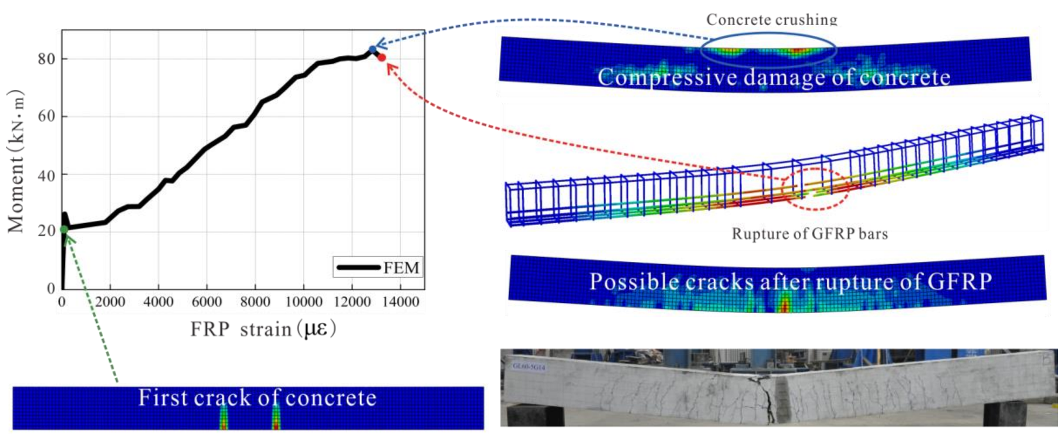

Figure 14. Crack patterns, strain of GFRP bars, and the final failure mode of FE model SLC–G–5#13.77.

4.1.4. FRP Rupture

The FE model for SLC–G–3#13.77 was used to demonstrate the FRP rupture failure mode. The progressive damage model, as mentioned in the previous section, entailed the sudden rupture of GFRP bars. Owing to its relatively high strength, the concrete at the top surface of midspan did not exhibit any compressive damage when the ultimate load was reached. Thus, the failure mode of FRP rupture was satisfactorily obtained (Figure 15).

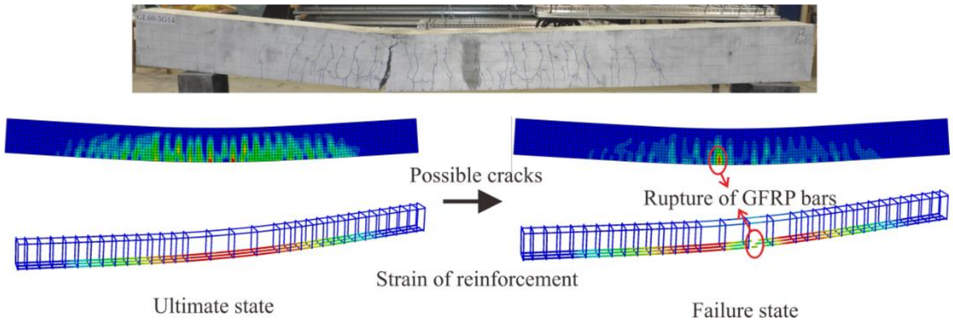

Figure 15. Crack patterns, strain of GFRP bars, and the final failure mode of FE model SLC–G–3#13.77.

4.2. *Deflection Behavior, Ultimate Capacity, and FRP Strain*

Comparisons between the experimental midspan deflections of the beams and the theoretical results based on the FE models are displayed in Figure 16. According to the curve segments divided in [10], generally, the experimental and measured deflections followed the same trend in the precracking and postcracking stages. For GFRP-reinforced beams that experienced concrete crushing, the FE models yielded a stage that corresponded to the crushing process, which was in agreement with the test results. However, the estimations with respect to the deflection value evidenced discrepancies in this stage. In the case of the steel reinforced beam LC–S–4#10.62 (Figure 16j), the FE model provided reasonable predictions during the entire loading period.

Based on Bischoff et al.'s recommendation [31], the 30% of M_u obtained by the test results was selected as the service load to evaluate the accuracy of the established FE models. Table 4 lists the Δ_s according to the FE models and the experimental-to-predicted Δ_s ($\Delta_{s,\mathrm{Exp}}/\Delta_{s,\mathrm{FEM}}$). The models predicted the Δ_s with a mean $\Delta_{s,\mathrm{Exp}}/\Delta_{s,\mathrm{FEM}}$ of 1.09 ± 0.19, while ACI 440.1R [33], CSA S806 [34], and GB 50608 [32] provided estimations with average $\Delta_{s,\mathrm{Exp}}/\Delta_{s,\mathrm{FEM}}$ values of 0.94 ± 0.38, 0.57 ± 0.26, and 1.97 ± 0.40, respectively, as calculated in [10]. The estimations based on the FE models closely matched the measured deflections at service load with small dispersion, which supported the validity of the developed FE model in predicting the stiffness of LWAC and SFLC beams reinforced with GFRP bars.

Table 4 summarizes the M_u computed by the FE method and compared the predictions with the experimental results. The established FE models yielded accurate M_u predictions with an average experimental-to-predicted ratio ($M_{u,\mathrm{Exp}}/M_{u,\mathrm{FEM}}$) of 1.04 ± 0.17. While the $M_{u,\mathrm{Exp}}/M_{u,\mathrm{FEM}}$ values that were obtained according to ACI 440.1R [33], CSA S806 [34], and GB 50608 [32] were 0.94 ± 0.38, 1.01 ± 0.39, 0.94 ± 0.16, as reported in [10]. In addition, as shown in Figure 17, the similar evolution of strain in GFRP reinforcement suggested that the definition of tension stiffening applied in this study was applicable for such beams.

However, the models for LC–G–6#9.87 and SLC–G–6#9.87 produced some relatively larger deviations in predicting the ultimate capacity and deflection of beams. The discreteness in the mechanical properties of the concrete and GFRP bars was responsible for this difference between the simulation and test results. Notwithstanding these errors, the whole moment–deflection responses and evolution of FRP strain still presented an acceptability of FE models.

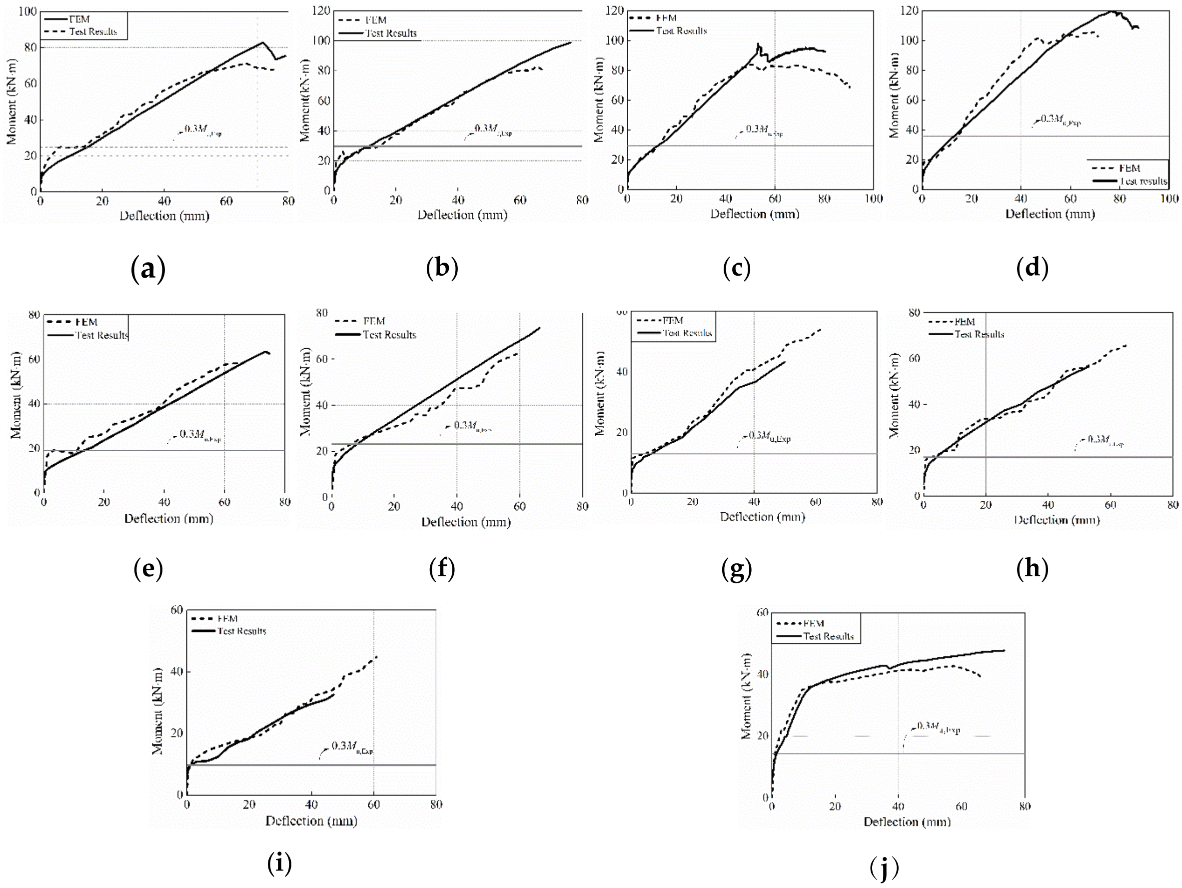

Figure 16. Comparison of moment-deflection curves: (**a**) LC–G–5#13.77; (**b**) SLC–G–5#13.77; (**c**) LC–G–8#13.77; (**d**) SLC–G–8#13.77; (**e**) LC–G–3#13.77; (**f**) SLC–G–3#13.77; (**g**) LC–G–6#9.87; (**h**) SLC–G–6#9.87; (**i**) LC–G–4#9.87; and (**j**) LC–S–4#10.62.

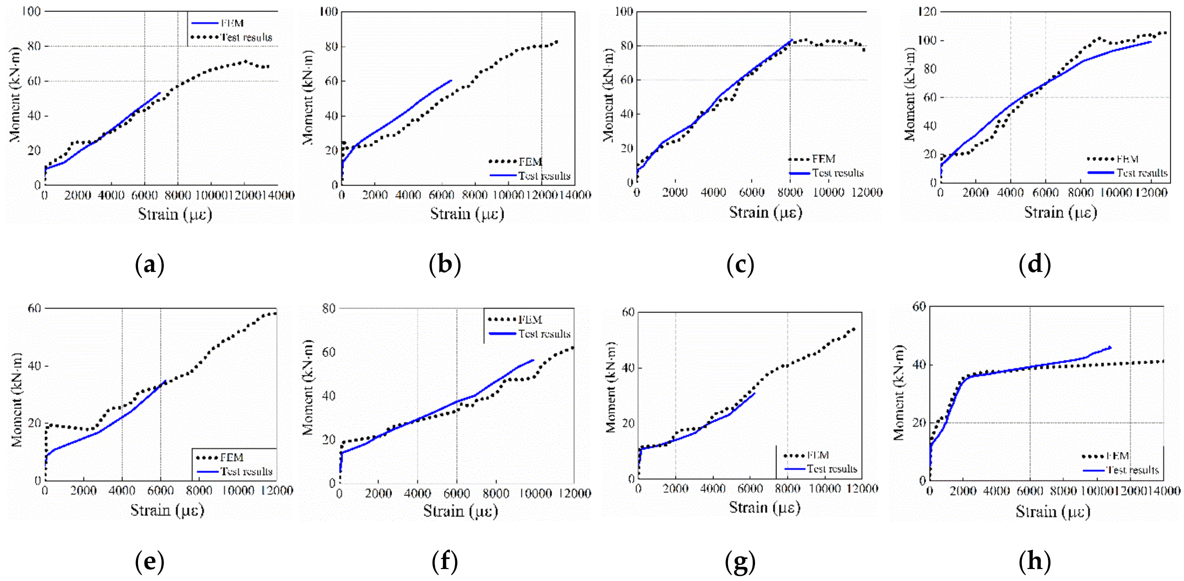

Figure 17. Comparison of moment-strain of GFRP bars: (**a**) LC–G–5#13.77; (**b**) SLC–G–5#13.77; (**c**) LC–G–8#13.77; (**d**) SLC–G–8#13.77; (**e**) LC–G–3#13.77; (**f**) SLC–G–3#13.77; (**g**) LC–G–6#9.87; and (**h**) LC–S–4#10.62.

The modeling and predictions of three specimens reinforced with GFRP bars yielding different failure modes, and the specimens without GFRP bars were analyzed to illustrate the results of the FE method. Figure 18 presents the historical energy of the four models. The kinetic energy of the four models was negligible; therefore, the influence of kinetic energy on the results was insignificant. Similarly, the results of all 10 models were not found to be greatly affected by kinetic energy, yet the diagrams for these were not presented owing to the length limitation.

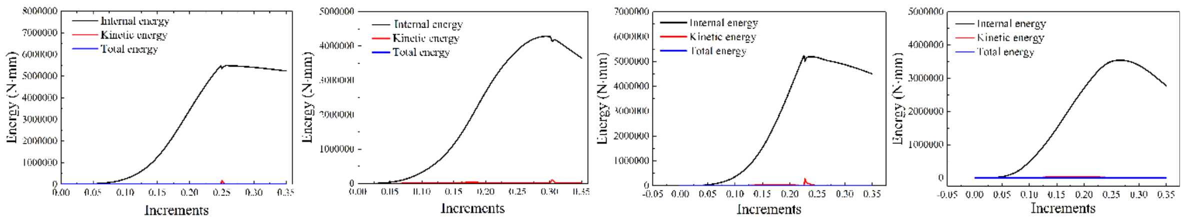

(**a**) (**b**) (**c**) (**d**)

Figure 18. Historical energy of models with different failure modes: (**a**) LC–G–5#13.77; (**b**) SLC–G–5#13.77; (**c**) SLC–G–3#13.77; and (**d**) LC–S–4#10.62.

5. Parametric Analysis

To further investigate the performance of SFLC beams reinforced with GFRP bars, the FE model for SLC–G–8#13.77 was selected as the control sample to conduct the parametric analysis with respect to the section height H, FRP reinforcement ratio ρ_f, and clear span length L.

5.1. Section Height

Figure 19 displays the evolution of the ultimate moment, deflection, and reinforcement strain. The detailed results of FE analysis are given in Table 5. As the H increased from 300 to 450 mm, the failure modes obtained by the FE method transformed from concrete crushing into balanced, which could be attributed to the reduction in the ρ_f. Specimens with H values of 350 mm, 400 mm, and 450 mm were all damaged due to balanced failure, indicating that the reinforcement ratio corresponding to balanced failure was actually a range instead of an exact value for certain materials. Although the same failure mode was obtained, there was a slight difference in the range of the crushed concrete. As expected, the range of the crushed concrete of specimens with an H value of 450 mm was slightly smaller than that of specimens with an H value of 350 mm, as illustrated in Figure 20.

Table 5. Predictions of FE models.

Series	H (mm)	ρ_f (%)	L (mm)	M_{cr} (kN·m)	M_u (kN·m)	Δ_s (mm)	Failure Mode
IV	300	2.66	3000	18.60	105.45	12.44	C.C
	350	2.66	3000	29.12	135.02	4.82	B.F
	400	2.66	3000	35.78	177.36	7.98	B.F
	450	2.66	3000	41.58	210.11	4.26	B.F
V	300	0.92	3000	18.96	63.21	1.40	FRP.R
	300	1.33	3000	18.44	84.12	2.71	B.F
	300	2.66	3000	18.60	105.45	12.44	C.C
	300	3.68	3000	18.58	112.64	3.39	C.C
VI	300	2.66	3000	18.60	105.45	14.60	C.C
	300	2.66	3600	18.18	99.98	13.18	C.C
	300	2.66	4200	17.76	104.49	19.92	C.C
	300	2.66	4800	16.09	102.38	27.58	C.C

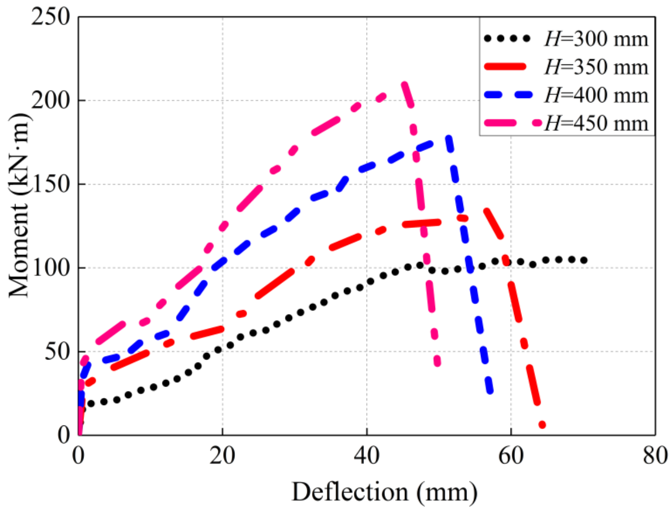

Figure 19. Influence of the section height.

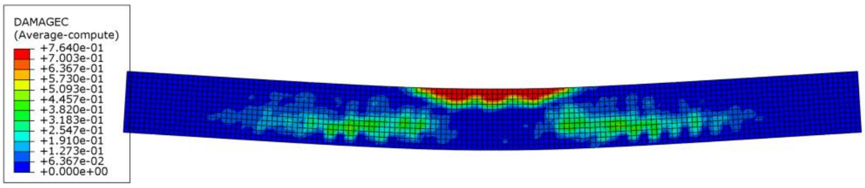

(**a**)

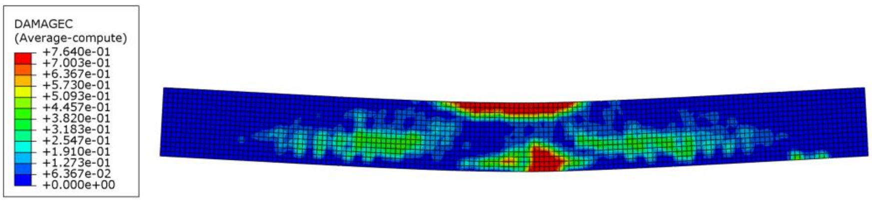

(**b**)

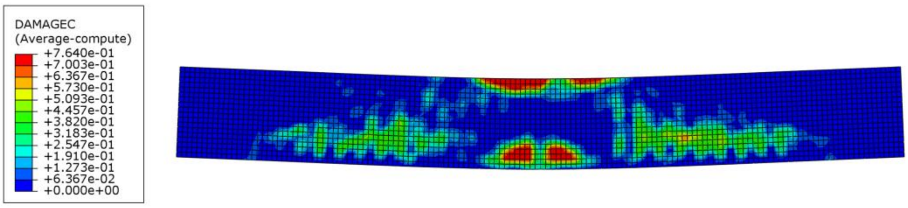

(**c**)

Figure 20. Failure modes obtained by FE method: (**a**) Concrete crushing of model with height of 300 mm; (**b**) Balanced failure of models with height of 350 mm; (**c**) Failure mode of model with height of 450 mm.

The increase of the H value was beneficial for the capacity of SFLC beams reinforced with GFRP bars, which was similar to the traditional RC beam. However, a minimum ρ_f was especially required for this kind of beam to avoid the unexpected rupture of GFRP bars. In terms of deflection, no direct relationship between the H and the Δ_s values was observed, since increasing the H increased the M_u and the stiffness simultaneously.

5.2. Reinforcement Ratio

The reinforcement ratio was varied from 0.92% to 3.68% to study the effects of the reinforcement ratio on the performance of SFLC beams reinforced with GFRP bars. Figure 21 presents the ultimate moment of FE models, and Table 5 gives the details of the simulated results.

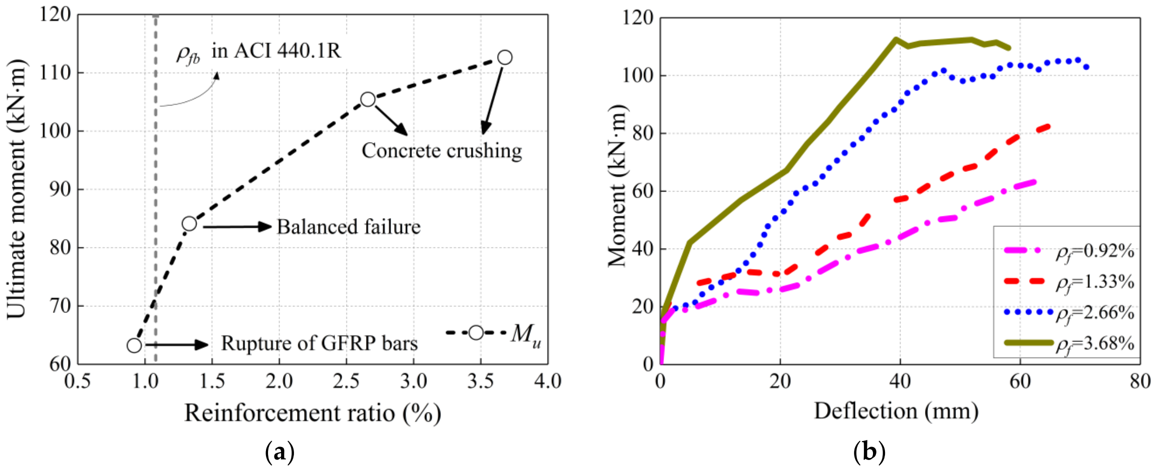

Figure 21. Influence of reinforcement ratio: (**a**) Ultimate capacity of finite-element (FE) models; (**b**) Moment–deflection response of FE models.

As can be seen in Figure 21, the ρ_f value of the model with balanced failure was higher than that given by ACI 440.1R [33]. Due to the destructive feature of FRP tension failure, the designers should adopt a factor to ensure concrete crushing of the beam, as 1.4 in ACI 440.1R [33]. Furthermore, the capacity of the beam was not increased by the reinforcement ratio linearly, so that it was necessary to determine the critical ratio for concrete crushing in order to make relatively full use of the materials' strength.

As shown in Table 5, the Δ_s first increased and then decreased with the increasing ρ_f. This result could be attributed to the fact that increasing the ρ_f had both positive and negative influences on the Δ_s, more specifically, improving the M_s as well as lowering the deflection simultaneously. For specimens with ρ_f values of 0.92% and 1.33%, their M_s were close to the cracking moment (M_{cr}), and thus led to very low Δ_s values. Nevertheless, their failure modes, including FRP rupture and balanced failure, were brittle and catastrophic. When further increasing the ρ_f to 2.66%, the failure mode changed to concrete crushing, and the Δ_s increased to 12.44 mm. It could be derived that the improvement in the stiffness failed to complement the increase in the M_s. Comparing specimens that failed due to concrete crushing (with ρ_f of 2.66% and 3.68%) revealed that the increase in ρ_f had an obvious effect on the reduction of deflection. The reason behind this behavior was that increasing the ρ_f did not significantly increase the flexural capacity M_s for this failure mode.

5.3. Length of Span L

Specimens with same shear span ratio but different L were studied according to the established FE model. Table 5 presents the M_u, Δ_s, and failure modes of the specimens with L values of 3000 mm, 3600 mm, 4200 mm, and 4800 mm. The Δ_s of the specimens and the deflection limit required by GB 50608 [32], L/200, are depicted in Figure 22. As expected, specimens with the same ρ_f but varied L values exhibited the same failure mode and similar M_u (M_s) values. The Δ_s was not linearly altered with the increase of span for beams with the same reinforcement ratio. This was consistent with the deflection equation based on the fundamental theory of material mechanics [34], in which the deflection was a quadratic function of L for a given moment. As the deflection limit was in proportion to the L, the Δ_s of specimens with larger values were more likely to exceed its limit. Intuitively, as displayed in Figure 22, the Δ_s values of beams with L that ranged from 3000 to 4200 mm were acceptable, while that of their counterpart with an L of 4800 mm was unconservative. Therefore, a larger reinforcement ratio was needed for SFLC beams reinforced with GFRP bars with larger span lengths according the current provisions.

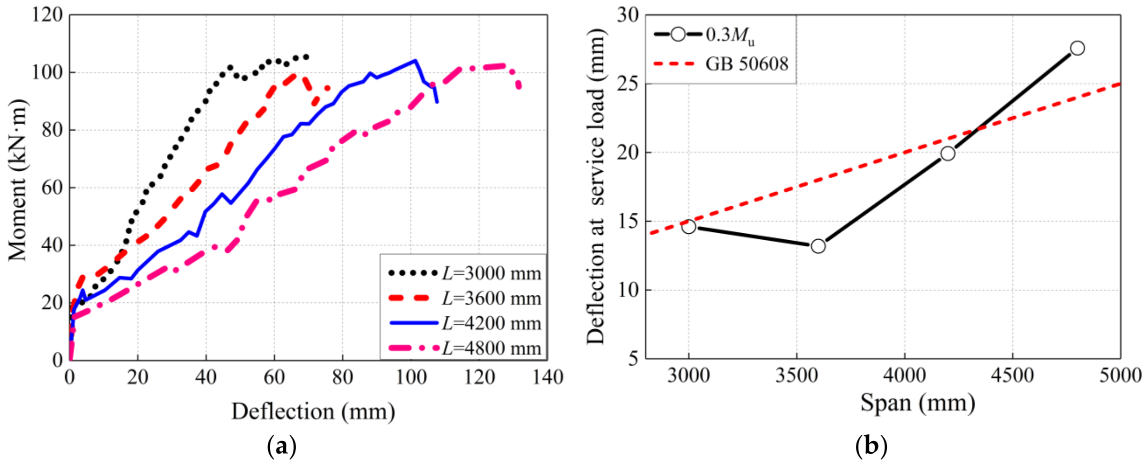

Figure 22. Influence of clear span length: (**a**) Moment–deflection response of FE models; (**b**) Δ_s of specimens with varied L.

6. Conclusions

In the present study, nonlinear FE models were established to simulate the behavior of LWAC and SFLC beams reinforced with GFRP bars. A dynamic explicit procedure together with a progressive model was employed to simulate the brittle failure of the beams. The validation of FE models was confirmed according to the experiments previously reported by the authors, and the influencing factors, including the height, reinforcement ratio, and length of span were discussed through the FE method. The following conclusions are drawn:

(1) The established FE models successfully obtained three failure modes of beams referring to the test results, namely concrete crushing, balanced failure, and FRP rupture. This confirmed that the constitutive models of LWAC and SFLC introduced in the FE model are efficient, and the inclusion of progressive damage into the properties of GFRP bars is capable of reflecting the rupture behavior. Moreover, the explicit procedure entails the uninterrupted calculation when brittle failures occurred.

(2) The FE models yielded accurate ultimate capacity predictions with an average experimental-to-predicted ratio of 1.04 ± 0.17. At service load, the estimated deflection closely matched the measured results with an average experimental-to-predicted ratio of 1.09 ± 0.19.

(3) The reinforcement ratio corresponding to balanced failure was higher than that given by code ACI 440.1R, which confirmed the necessity of the amplification factor of a balanced reinforcement ratio to ensure the concrete crushing of the beam.

(4) For specimens that failed due to concrete crushing, the increase in the FRP reinforcement ratio did not significantly improve the ultimate capacity, but it did have an obvious effect on the reduction of deflection at service load.

(5) The increase rate of the deflection at service load was higher for GFRP-reinforced beams with larger clear span lengths. Therefore, a greater reinforcement ratio is needed for beams when the span length is increased.

Author Contributions: Conceptualization, T.W.; Data curation, Y.S. and Y.L.; Formal analysis, Y.S. and Y.L.; Funding acquisition, T.W. and X.L.; Investigation, Y.L., X.L. and H.L.; Supervision, T.W.; Visualization, Y.S. and Y.L.; Writing—original draft, Y.S. and Y.L.; Writing—review and editing, Y.S., X.L. and T.W.

Funding: This research was funded by the National Natural Science Foundation of China (No. 51708036, 51878054, and 51908041), the Natural Science Foundation of Shaanxi Province (Key Research and Development Program) (No. 2018ZDCXL-SF-03-03-02) and Natural Science Foundation of Shaanxi Province (No. 2018JQ5005).

Conflicts of Interest: The authors declare there is no conflict of interest regarding the publication of this paper.

References

1. Gao, Y.L.; Chao, Z. Experimental study on segregation resistance of nanoSiO2 fly ash lightweight aggregate concrete. *Constr. Build. Mater.* **2015**, *93*, 64–69. [CrossRef]
2. Sohel, K.M.A.; Al-Jabri, K.; Zhang, M.H.; Liew, J.Y.R. Flexural fatigue behavior of ultra-lightweight cement composite and high strength lightweight aggregate concrete. *Constr. Build. Mater.* **2018**, *173*, 90–100. [CrossRef]
3. Gao, J.M.; Wei, S.; Keiji, M. Mechanical properties of steel fiber-reinforced, high-strength, lightweight concrete. *Cem. Concr. Compos.* **1997**, *19*, 307–313. [CrossRef]
4. Karayannis, C.G. Nonlinear analysis and tests of steel-fiber concrete beams in torsion. *Struct. Eng. Mech.* **2000**, *9*, 323–338. [CrossRef]
5. Campione, G. Flexural and shear resistance of steel fiber–reinforced lightweight concrete beams. *J. Struct. Eng.* **2013**, *140*, 04013103. [CrossRef]
6. Grabois, T.M.; Guilherme, C.C.; Toledo Filho, R.D. Fresh and hardened-state properties of self-compacting lightweight concrete reinforced with steel fibers. *Constr. Build. Mater.* **2016**, *104*, 284–292. [CrossRef]
7. Li, J.J.; Wan, C.J.; Niu, J.G.; Wu, L.F.; Wu, Y.C. Investigation on flexural toughness evaluation method of steel fiber reinforced lightweight aggregate concrete. *Constr. Build. Mater.* **2017**, *131*, 449–458. [CrossRef]
8. Libre, N.A.; Shekarchi, M.; Mahoutian, M.; Soroushian, P. Mechanical properties of hybrid fiber reinforced lightweight aggregate concrete made with natural pumice. *Constr. Build. Mater.* **2011**, *25*, 2458–2464. [CrossRef]
9. Blaznov, A.N.; Krasnova, A.S.; Krasnov, A.A.; Zhurkovsky, M.E. Geometric and mechanical characterization of ribbed FRP rebars. *Polym. Test.* **2017**, *63*, 434–439. [CrossRef]
10. Wu, T.; Sun, Y.J.; Liu, X.; Wei, H. Flexural behavior of steel fiber–reinforced lightweight aggregate concrete beams reinforced with glass fiber–reinforced polymer bars. *J. Compos. Constr.* **2019**, *23*, 04018081. [CrossRef]
11. Karayannis, C.G.; Kosmidou, P.K.; Chalioris, C.E. Reinforced concrete beams with carbon fiber reinforced polymer bars Experimental study. *Fibers* **2018**, *6*, 99. [CrossRef]
12. Kosmidou, P.-M.K.; Chalioris, C.E.; Karayannis, C.G. Flexural/shear strength of RC beams with longitudinal FRP bars-An analytical approach. *Comput. Concr.* **2018**, *22*, 573–592. [CrossRef]
13. Gribniak, V.; Kaklauskas, G.; Torres, L.; Daniunas, A.; Timinskas, E.; Gudonis, E. Comparative analysis of deformations and tension-stiffening in concrete beams reinforced with GFRP or steel bars and fibers. *Compos. Part B-Eng.* **2013**, *50*, 158–170. [CrossRef]
14. Zhu, H.T.; Cheng, S.; Gao, D.; Neaz, S.M.; Li, C. Flexural behavior of partially fiber-reinforced high-strength concrete beams reinforced with FRP bars. *Constr. Build. Mater.* **2018**, *161*, 587–597. [CrossRef]
15. Abed, F.; Alhafiz, A.R. Effect of basalt fibers on the flexural behavior of concrete beams reinforced with BFRP bars. *Compos. Struct.* **2019**, *215*, 23–34. [CrossRef]
16. De Domenico, D.; Pisano, A.A.; Fuschi, P. A FE-based limit analysis approach for concrete elements reinforced with FRP bars. *Compos. Struct.* **2014**, *107*, 594–603. [CrossRef]
17. Mohamed, O.A.; Khattab, R.; Al Hawat, W. Numerical Study on Deflection Behaviour of Concrete Beams Reinforced with GFRP Bars. *IOP Conf. Ser. Mater. Sci. Eng.* **2017**, *245*, 032065. [CrossRef]
18. Earij, A.; Alfano, G.; Cashell, K.; Zhou, X. Nonlinear three–dimensional finite–element modelling of reinforced–concrete beams: Computational challenges and experimental validation. *Eng. Fail. Anal.* **2017**, *82*, 92–115. [CrossRef]
19. Dassault Systèmes. ABAQUS 6.14 Analysis User's Guide, Materials. USA. 2014. Available online: http://ivt-abaqusdoc.ivt.ntnu.no:2080/v6.14/books/usb/default.htm (accessed on 30 October 2019).
20. Lubliner, J.; Oliver, J.; Oller, S.; Oñate, E. A plastic-damage model for concrete. *Int. J. Solids Struct.* **1989**, *25*, 299–326. [CrossRef]
21. Lee, J.; Gregory, L.F. Plastic-damage model for cyclic loading of concrete structures. *J. Eng. Mech.* **1998**, *124*, 892–900. [CrossRef]

22. Liu, X.; Wu, T.; Yang, L. Stress-strain relationship for plain and fibre-reinforced lightweight aggregate concrete. *Constr. Build. Mater.* **2019**, *225*, 256–272. [CrossRef]
23. Carreira, D.J.; Chu, K.-H. Stress-strain relationship for plain concrete in compression. *J. Proc.* **1985**, *82*, 797–804.
24. Hillerborg, A.; Mats, M.; Petersson, P.-E. Analysis of crack formation and crack growth in concrete by means of fracture mechanics and finite elements. *Cem. Concr. Res.* **1976**, *6*, 773–781. [CrossRef]
25. ACI 440.3R. *Guide Test Methods for Fiber-Reinforced Polymers (FRPs) for Reinforcing or Strengthening Concrete Structures*; American Concrete Institute: Farmington Hills, MI, USA, 2012.
26. ASTM E8/E8M. *Standard Test Methods for Tension Testing of Metallic Materials*; ASTM International: West Conshohocken, PA, USA, 2016.
27. Yang, J.M.; Min, K.H.; Shin, H.O.; Yoon, Y.S. Effect of steel and synthetic fibers on flexural behavior of high-strength concrete beams reinforced with FRP bars. *Compos. Part B-Eng.* **2012**, *43*, 1077–1086. [CrossRef]
28. Ovitigala, T.; Ibrahim, M.A.; Issa, M.A. Serviceability and ultimate load behavior of concrete beams reinforced with basalt fiber-reinforced polymer bars. *ACI Struct. J.* **2016**, *113*, 757–768. [CrossRef]
29. Goldston, M.W.; Remennikov, A.; Sheikh, M.N. Flexural behaviour of GFRP reinforced high strength and ultra high strength concrete beams. *Constr. Build. Mater.* **2017**, *131*, 606–607. [CrossRef]
30. Issa, M.S.; Metwally, I.M.; Elzeiny, S.M. Influence of fibers on flexural behavior and ductility of concrete beams reinforced with GFRP rebars. *Eng. Struct.* **2011**, *33*, 1754–1763. [CrossRef]
31. Bischoff, P.H.; Gross, S.; Ospina, C.E. The story behind proposed changes to ACI 440 deflection requirements for FRP-reinforced concrete. *Spec. Publ.* **2009**, *264*, 53–76.
32. GB 50608. *Technical Code for Infrastructure Application of FRP Composites*; China Planning Press: Beijing, China, 2010.
33. ACI 440.1R. *Guide for the Design and Construction of Structural Concrete Reinforced with Fiber-Reinforced Polymer Bars*; American Concrete Institute: Farmington Hills, MI, USA, 2015.
34. CSA S806. *Design and Construction of Building Structures with Fibre-Reinforced Polymers*; Canadian Standards Association: Toronto, ON, Canada, 2012.